

On-chip phased interdigital metamaterials enable versatile manipulation of surface acoustic waves, microfluids, and micro/nano-objects

Received: 15 February 2025

Accepted: 8 November 2025

Published online: 08 December 2025

 Check for updates

Jiali Li^{1,4}, Luyu Bo^{1,4}, Teng Li¹, Liang Shen¹, Chongpeng Qiu¹, Yingshan Du²,
Shujie Yang³✉ & Zhenhua Tian¹✉

Surface acoustic waves (SAWs) offer great potential for quantum information processing, optomechanics, acoustofluidics, and acoustic tweezers. However, existing SAW chips lack the ability to control SAWs in a manner similar to current metamaterials, which can achieve versatile subwavelength-resolution manipulation of bulk acoustic waves. This study presents on-chip phased interdigital metamaterials (PIMs) featuring customized interdigital electrodes whose geometries are encoded with deep-subwavelength-resolution phase profiles, enabling versatile transformation of SAWs and manipulation of fluids and micro/nano-objects. Our on-chip PIMs can transform forward SAWs into waves with desired wavefronts and energy patterns, such as SAWs propagating in a specified direction, a SAW jet with energy confined in a wavelength, and twin jets. They also enable “diode-like” SAW transmission, allowing for routing the information carried by SAWs along a forward pathway while blocking backward communication. Additionally, SAWs generated by PIMs exhibit unique energy patterns, allowing for versatile active control of fluid streaming and micro/nano-object distributions.

Surface acoustic wave (SAW) technologies, employing nanoscale “earthquakes” on piezoelectric chips, have shown great potential in various fields such as quantum acoustics^{1–4}, optomechanics^{5–9}, wireless communication^{10–13}, and acoustofluidics^{14–19}. In quantum acoustics, a superconducting qubit can be coupled with SAWs, exhibiting non-linear SAW reflection and relaxation of an excited qubit through SAW emission⁴. In optomechanics, SAWs can resonantly excite an optomechanical cavity^{5,6} and precisely trigger single-photon generation by controlling the injection of electrons and holes into quantum dots⁹. For communication systems, SAW-based filters, duplexers, and multiplexers play critical roles^{10,11}. In recent years, SAWs have increasingly found numerous applications in life sciences^{20–25}, including bioparticle

detection with SAW-based biosensors^{26–28}, processing small volumes of bioliquids with SAW-based acoustofluidic devices^{29–34}, and contactless manipulation of tiny bio-samples ranging from nano- to millimeter scales (e.g., zebrafish^{35,36}, cells^{37–42}, exosomes^{43–45}, and nucleic acids⁴⁴) using SAW-based acoustic tweezers.

Despite advances in SAW technologies, multiple challenges remain. Interdigital transducers (IDTs) with parallel straight electrodes and concentric arc-shaped electrodes have long been predominantly used for generating straight-wavefront and focused SAWs^{23–26,46,47}, respectively. Beyond these traditional designs, IDTs with various unique electrode geometries have been developed to achieve different functionalities – for example, focused IDTs with electrode geometries

¹Department of Mechanical Engineering, Virginia Tech, Blacksburg, VA 24060, USA. ²Department of Biomedical Engineering and Science, Virginia Tech, Blacksburg, VA 24060, USA. ³Department of Mechanical Engineering and Applied Mechanics, University of Pennsylvania, Philadelphia, PA 19104, USA. ⁴These authors contributed equally: Jiali Li, Luyu Bo. ✉e-mail: shujie.yang@seas.upenn.edu; tianz@vt.edu

derived from slowness curves for improved SAW focusing^{48–51}, spiral-shaped IDTs for generating acoustic vortices^{19,42,52}, and angularly slanted IDTs capable of steering SAW direction via frequency tuning^{53,54}. However, a generalized approach for designing IDTs with complex-shaped interdigital electrodes that can generate SAWs with user-defined wavefronts and energy patterns remains lacking, thus limiting the development of customized SAW devices tailored to generate optimal SAW fields for specific application needs. Moreover, few studies have developed metamaterials capable of transforming incident SAWs into waves with targeted propagation directions, wavefront shapes, and energy profiles, and no SAW metamaterial device to date can simultaneously perform such transformations and enable “diode-like” SAW information delivery. Although some studies have explored mechanisms that use components (*e.g.*, thin film transistors, magnetoelastic coupling layers, etc.) placed in the SAW path to modulate transmitted SAWs^{55–65}, integrating these components into large arrays for subwavelength-resolution SAW field transformation remains challenging due to the difficulty of scaling down the complex intermediate modulators to subwavelength dimensions and/or fabricating arrays that incorporate many of them. Recently, Xu et al. introduced sawtooth-shaped metasurfaces bonded to a substrate for SAW deflection⁶⁶, and Wang et al. demonstrated both SAW focusing and deflection by depositing metasurfaces composed of pillar arrays with varied designs onto a substrate⁶⁷. However, these approaches require complex fabrication processes due to the addition of extra microstructures, and their functionalities remain limited to SAW deflection and/or focusing. Third, in applied acoustics, a long acoustic jet with energy highly focused within a wavelength shows great potential for acoustic sensing and diagnostics^{68–70}, and acoustic twin beams with energy confined in paired beams enable unique acoustic tweezers for single-object manipulation^{71–73}. However, no studies have realized on-chip SAW jets that could benefit SAW sensor development or explored SAW twin beams that might enable novel SAW tweezers for arranging micro/nano-objects.

To address these gaps, this study presents phased interdigital metamaterials (PIMs) for multi-mode manipulation of on-chip SAWs, microfluids, and micro/nano-objects, such as transforming SAW wavefronts and energy fields, generating unique vortex streaming, and arranging micro/nano-objects into various patterns. Compared to traditional simple-configuration IDTs, the PIMs are composed of complex-shaped electrodes encoded with deep-subwavelength-resolution, position-dependent phase profiles, thus allowing for generating SAWs with tailored wavefronts and energy fields. These PIM offers a unique approach for developing SAW chips that can steer incident SAWs and transform them into waves with diverse wavefronts and energy patterns—without relying on wave interactions with complex-shaped microstructures (such as the micropillar arrays and sawtooth microstructures used in recently developed metasurfaces^{66,67}), which require intricate microfabrication processes to be integrated onto the substrate. Compared to those metasurfaces designed for SAW deflection and/or focusing^{66,67}, our PIM-based chip can achieve more complex SAW field transformations and enable “diode-like” routing of information carried by SAWs. Through validation experiments, our PIM-based chips were successfully demonstrated to transform forward-direction SAWs into waves propagating in desired directions, long single SAW jets, as well as a pair of SAW jets (*i.e.*, twin SAW jets). These chips also successfully routed the information carried by SAWs along the forward pathway while forbidding information delivery in the backward direction. Furthermore, as our PIMs can generate SAWs with unique energy patterns (*e.g.*, pseudo-standing SAWs, single SAW jets, and twin jets), they enable appealing acoustofluidic functions for actively controlling fluids and micro/nano-objects. These functions were validated by arranging microparticles into

various patterns, aligning multi-walled carbon nanotubes (MWCNTs), generating counter-chirality streaming vortices, as well as driving the motions of nano-objects.

Results

On-chip phased interdigital metamaterials (PIMs) for manipulating surface acoustic waves (SAWs), fluids, and micro/nano-objects

The PIM is inspired by acoustic holography, which leverages a wave transformation module (*e.g.*, an acoustic lens or metamaterial) containing customized, position-dependent phase information to modulate acoustic waves generated from a transducer (*e.g.*, a piezoelectric plate)^{74–76}, as illustrated in Fig. 1a. The commonly used acoustic holography approach struggles to manipulate high-frequency SAWs propagating along a piezoelectric wafer’s surface due to the challenges in developing and manufacturing arrays of microscale, subwavelength elements capable of inducing desired phase shifts in a range of 0 to 2π rad. To address these challenges, we developed PIMs that integrate the wave transformation and generation modules by encoding the desired position-dependent, subwavelength-resolution phase information into the shapes of the PIMs’ microscale interdigital electrodes, as illustrated in Fig. 1a (right). This approach allows for engineering both the SAW wavefronts and energy distributions by carefully designing the PIM’s interdigital electrode pattern with subwavelength resolution. Based on this mechanism, four example PIMs have been designed to generate SAWs propagating in a desired direction (Fig. 1b), pseudo-standing SAWs (Fig. 1c) with an energy pattern like that of standing SAWs generated by a pair of parallel IDTs, a long SAW jet with most SAW energy focused in a long narrow beam (Fig. 1d), and SAW twin jets with most SAW energy confined in a pair of long narrow beams (Fig. 1e).

PIMs can also be used to develop SAW chips that transform incident SAWs and achieve “diode-like” unidirectional transmission of the information carried by SAWs. As illustrated in Fig. 1f, by integrating four key modules, including a typical straight-electrode IDT, a lossy material (*e.g.*, high-damping paste or polymer), a gain module (*e.g.*, one-way amplification circuit), and a PIM, we have developed a SAW metamaterial chip capable of transforming forward-propagating SAWs into waves with desired wavefronts and energy distributions. For example, when straight-wavefront SAWs incoming from the left side of the chip reach the straight-electrode IDT, an electrical signal is generated from the IDT. This signal is then amplified by a one-way amplification circuit and sent to the PIM on the right side of the lossy material. This allows the incident straight-wavefront SAWs to be transformed into SAWs with desired wavefronts and energy distributions, depending on the PIM’s electrode pattern. In contrast, the information of SAWs incoming from the right side of the metamaterial cannot be transmitted to the left side, as the amplification circuit ensures one-way transmission and amplification of the electrical signal. The lossy material is also critical to achieving “diode-like” unidirectional transmission of SAW information, as it absorbs SAWs arriving from both sides of the piezoelectric substrate and breaks the wave path through the substrate.

In addition to manipulating SAW propagation, PIMs can facilitate the development of acoustic tweezers for manipulating micro/nano-objects, as well as on-chip flow control devices that can generate versatile fluid streaming fields. On one hand, using a pair of PIMs, customized distributions of acoustic potential valleys can be generated to trap tiny objects using acoustic radiation forces and arrange them in various patterns, such as tilted parallel-line-like and two-dimensional (2D) lattice-like arrangements (Fig. 1g, h). With this design approach, infinite customized SAW energy patterns can be generated to construct diverse object patterns by carefully designing the electrode shapes of PIMs through the encoding of desired phase profiles. On the other hand, traveling SAWs from PIMs can generate acoustic streaming in a liquid layer on the SAW substrate, further inducing drag forces on

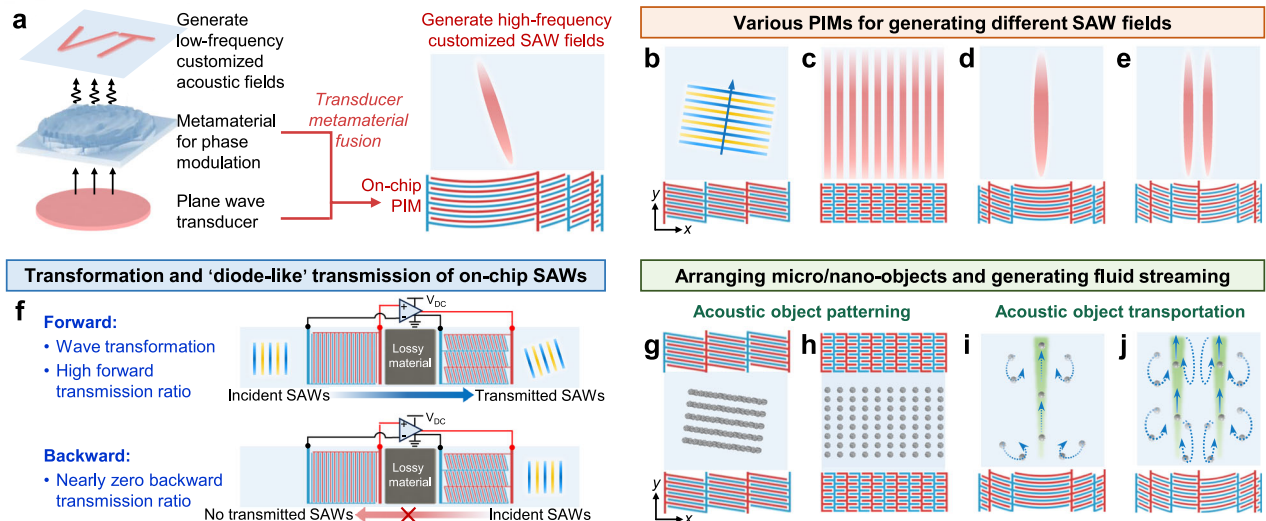


Fig. 1 | Schematics illustrating the designs and mechanisms of phased interdigital metamaterials (PIMs) for manipulating on-chip surface acoustic waves (SAWs), fluids, and micro/nano-objects. **a** Schematic of a PIM. Its mechanism is inspired by acoustic holography that uses a wave transformation module (e.g., a lens or metamaterial) containing required position-dependent phase information for modulating acoustic waves generated from a plane-wave transducer. Our PIM integrates the wave transformation and generation modules, by encoding the required subwavelength-resolution position-dependent phase information into the shapes of the microscale interdigital electrodes deposited on piezoelectric wafers.

b–e Four different designs of PIMs for generating SAWs propagating a desired direction, pseudo-standing SAWs, a long SAW jet, and SAW twin jets, respectively. **f** Schematic illustrating the mechanism of a metamaterial that is based on a PIM for enabling the functions of transforming on-chip SAWs and “diode-like” transmission of SAW information. **g, h** Schematic illustrating the function of arranging micro-objects using the acoustic radiation force generated by a PIM. **i, j** Schematic illustrating the function of driving micro/nano-object motions using acoustic streaming generated by a PIM. The yellow and blue parallel lines in **(b)** and **(f)** represent SAW wavefronts, while the SAW intensity patterns in **(a)** and **(b)** are illustrated in red.

tiny objects to transport them along streamlines. PIMs open a route for generating customized fluid streaming fields, as the PIMs’ electrode configurations can be engineered to generate various traveling SAW fields. For instance, a PIM designed to generate a long narrow SAW beam can produce a jet flow accompanied by multiple pairs of counter-chirality vortices on different sides of the jet flow (Fig. 1i). When customized to generate two long narrow SAW beams, two fluid jets accompanied by more pairs of counter-chirality vortices can be generated (Fig. 1j).

To support the development of PIMs, we established an analytical model (see Supplementary Note 1 and Supplementary Fig. 1) to quickly predict SAW fields generated by PIMs. Moreover, we have performed laser vibrometry-based SAW field visualization experiments to validate the ability of PIMs to generate SAWs with different wavefronts and energy patterns. Furthermore, using our PIMs, we have developed SAW metamaterial chips and experimentally validated their functions of transforming incident SAWs and performing “diode-like” transmission of SAW information. In addition, through a series of acoustofluidic experiments, we have demonstrated the capability of PIMs to generate acoustic streaming and arrange the distributions of micro/nano-objects. The key experimental results, along with the related data analysis and discussion, are given below.

Generation of versatile surface acoustic wave (SAW) fields

The shape of a PIM’s interdigital electrode is critical for generating SAWs with the desired frequency, wavefront shape, and energy pattern. Based on our proposed approach, which encodes the desired subwavelength-resolution spatially varying phase information into the electrode shape, we have developed multiple PIMs (see Supplementary Figs. 2 and 3 for configurations) to generate customized SAWs, such as tilted SAWs propagating in a desired direction and pseudo-standing SAWs. The mathematical descriptions of electrode shapes are provided in Supplementary Note 2. To characterize the PIMs, we acquired their generated SAW displacement and energy fields using a laser vibrometry system (Supplementary Fig. 4) and

further analyzed the generated SAW field’s wavenumber spectrum in the k_x - k_y domain.

To generate SAWs propagating in a direction of $\mathbf{e}_\theta = (\cos \theta, \sin \theta)$ (illustrated in Supplementary Fig. 2a), the PIM’s electrode shape should be encoded with a spatial-varying phase profile having a constant gradient $-\omega \cot \theta / c_{SAW}(\theta)$, where ω is the angular frequency and $c_{SAW}(\theta)$ is a direction-dependent SAW velocity. For example, when using a PIM (illustrated in Fig. 2b) encoded with a gradient phase profile shown in Supplementary Fig. 3b (top), the laser-measured SAW displacement field in Fig. 2e shows tilted wavefronts perpendicular to the SAW propagation direction $\theta = 80$ deg. This is also confirmed by the wavenumber analysis result in Fig. 2h, showing a high-intensity wavenumber spot in 80 deg in the k_x - k_y domain. In contrast, SAWs generated by a traditional straight-electrode IDT propagate in the 90 deg direction (Fig. 2d) and have a high-intensity wavenumber spot in 90 deg in the k_x - k_y domain (Fig. 2g). Additionally, the simulation results agree well with the experimental results (Fig. 2d–f), successfully validating our analytical model, which is for quickly predicting SAWs generated by PIMs with complex-shaped interdigital electrodes and guiding the PIM design and optimization.

By encoding the electrode shape with a phase profile in Supplementary Fig. 3c, which alternates between 0 and π rad with a spatial period of Δd , we developed a PIM to generate pseudo-standing SAWs. Details of the phase profile expression and PIM design can be found in Supplementary Note 2 and Supplementary Fig. 2b. For validation, we manufactured a PIM and performed laser-based SAW field characterization. The measured SAW intensity field (Fig. 2f, right) is similar to the intensity fields of standing SAWs generated by a pair of parallel IDTs, and thus the SAWs generated by our PIM are referred to as ‘pseudo-standing SAWs’ in this study. From the measured intensity field, it is evident that the x -direction spacing between adjacent intensity peaks is $\Delta d/2$, which depends on the design of the PIM rather than the generated SAW’s wavelength (λ). Moreover, this spacing is the same as the peak spacing in regular standing SAWs created by the interference of SAWs carrying wavenumbers of $\pm 2\pi/\Delta d$ generated at a

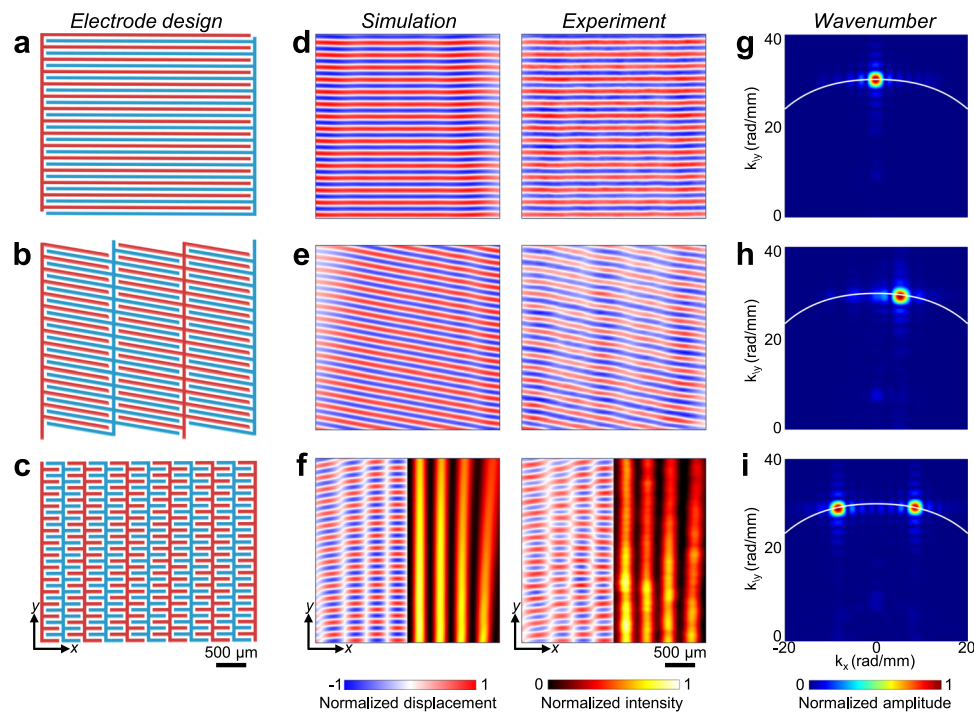


Fig. 2 | Experimental results for the generation of different high-frequency surface acoustic wave (SAW) fields on piezoelectric chips. **a–c** Exact electrode configurations of different interdigital transducers (IDTs). **d–f**, left SAW fields simulated by our analytical model. **d–f**, right SAW fields experimentally acquired by a laser Doppler vibrometer. **g–i** Wavenumber spectra of the generated SAW fields.

The white curves represent the theoretical wavenumber contour at 18.8 MHz. The first row gives the results of a traditional straight-electrode IDT. The second and third rows give results of phased interdigital metamaterials (PIMs) that can generate SAWs propagating in the 80 deg direction and pseudo-standing SAWs, respectively.

frequency $f = c_{SAW}(\theta)/\Delta d$. To further analyze the ‘pseudo-standing SAWs’, the acquired SAW field is transformed to a wavenumber spectrum in the k_x - k_y domain. The experimental wavenumber spectrum in Fig. 2i clearly shows two high-intensity spots symmetric to the k_y -axis. Our experimental results in the x - y and k_x - k_y domains prove the effectiveness of generating ‘pseudo-standing SAWs’ using only a PIM to generate traveling SAWs propagating in one direction, rather than the traditional method of using multiple IDTs to generate counter-propagating SAWs.

Generation of long narrow surface acoustic wave (SAW) jets

In addition to generating SAWs propagating in a desired direction and pseudo-standing SAWs, we have developed and validated PIMs (illustrated in Fig. 3a–d) for generating single long SAW jets and twin jets. An acoustic jet is a highly focused acoustic beam with a long beam length in the wave propagation direction while maintaining a subwavelength-scale width^{68–70}, which is defined by the distance between the beam’s full width at half maximum (FWHM) points illustrated in Supplementary Fig. 5. However, few methods can generate one or multiple long SAW jets on piezoelectric chips. Our developed PIMs overcome this limitation, enabling the generation of a long SAW jet and a pair of jets (*i.e.*, twin jets) at high frequencies, such as tens of megahertz. Moreover, key parameters of a SAW jet, such as beam length, orientation, and center position, can be customized by carefully designing the PIM’s electrode configuration.

The key to generating a long SAW jet is to optimize the PIM’s electrode shape so that the PIM can generate a series of focused SAWs whose focal points gradually change from $\mathbf{x}_F(1)$ to $\mathbf{x}_F(N)$ as illustrated in Supplementary Fig. 5. Using this approach, a long SAW jet with an energy profile ranging from $\mathbf{x}_F(1)$ to $\mathbf{x}_F(N)$ can be generated, as confirmed by the alignment of the generated SAW jet with the focal points shown in Supplementary Fig. 6. Moreover, SAW jets can exhibit different shapes by customizing PIM design parameters (*e.g.*, the number

of electrodes N , device span W , focal length d_c , and beam center shift Δs), as demonstrated by the simulation results in Supplementary Fig. 7, which also reveal how these parameters affect beam width (W_b). The results show that the beam width gradually increases with increasing focal length and/or decreasing device span. When the number of electrodes is small (*e.g.*, $N = 2$), this relationship aligns with the prediction $W_b = 1.02 \lambda d_c / W_c$, which is commonly used to estimate the beam widths of focused ultrasound transducers^{77,78}. Second, shifting the jet away from the device centerline toward the edge (*i.e.*, increasing Δs) results in a gradual increase in beam width. Third, as the number of electrodes increases, the beam width initially increases and then reaches a plateau. Additionally, by appropriately selecting the design parameters, subwavelength-scale beam widths can be achieved. These relationships observed from simulation results provide valuable guidance for optimizing PIM designs.

For experimental validation, we fabricated three PIMs, whose electrode shapes were designed based on phase profiles in Supplementary Fig. 3d–f, for generating single long SAW jets with different energy distributions (see Fig. 3a–c). When using a PIM (Fig. 3a) designed with focal points close to its electrodes, the measured SAW displacement and energy fields (Fig. 3e, i) clearly show a long SAW jet near the electrodes along the PIM’s centerline. When using a PIM (Fig. 3b) designed with focal points far from the electrodes, a long SAW jet far from the PIM electrodes is generated, as shown by the measured SAW displacement and energy fields (Fig. 3f and j). We also showed the ability to generate an off-center SAW jet (see Fig. 3g and k) by using a PIM whose focal points offset from the PIM centerline. To further analyze the generated SAW jets, the multi-dimensional Fourier transform was applied to the acquired wavefields to reveal their wavenumber components. Compared to the unfocused SAW’s spectrum (Fig. 2g) with only a high-intensity spot, the SAW jets generated along the centerline have wavenumber components widely and symmetrically spread in the $\pm k_x$ directions (Fig. 3m, n). When a SAW jet is left

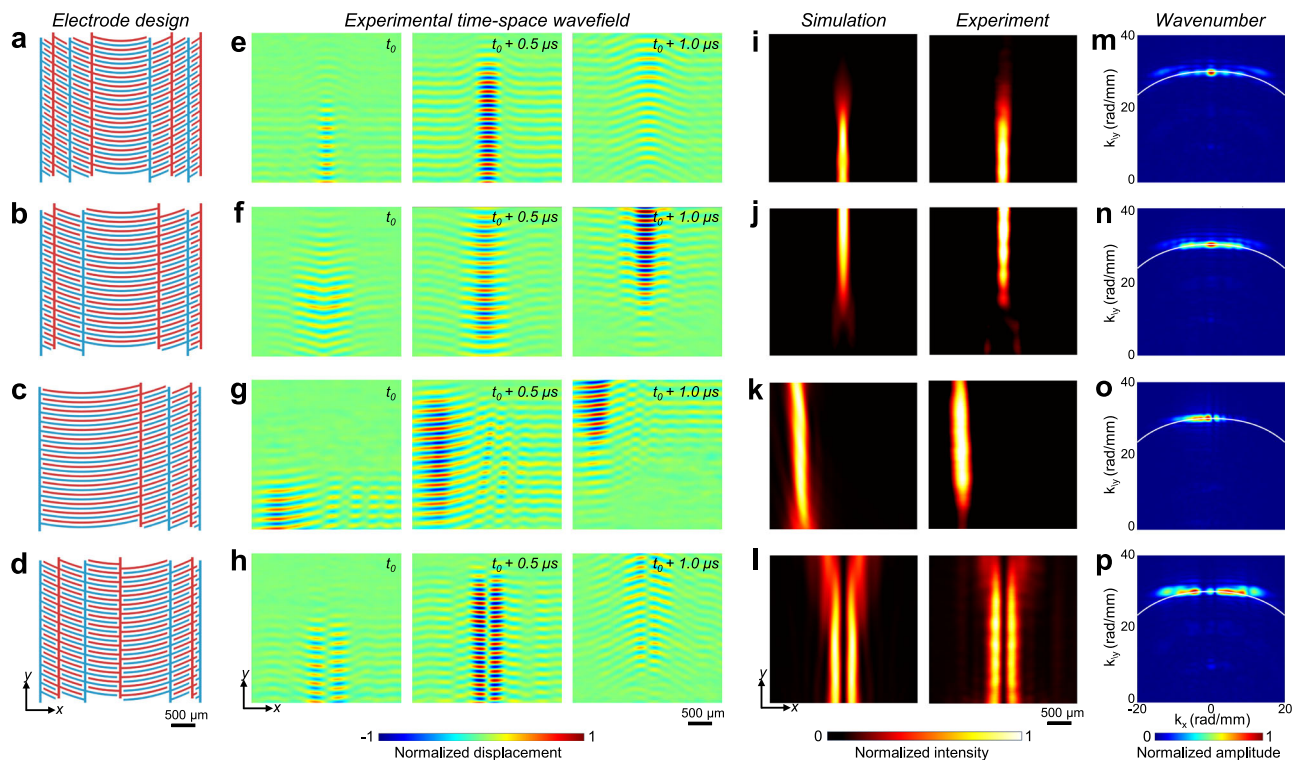


Fig. 3 | Experimental results for the generation of different high-frequency surface acoustic wave (SAW) energy beams on piezoelectric chips. a–d Exact electrode configurations of the used phased interdigital metamaterials (PIMs). **e–h** Experimentally acquired on-chip SAW fields at different times after excitation. **i–l**, left SAW energy fields simulated by our analytical model. **i–l**, right SAW energy

fields experimentally acquired by a laser Doppler vibrometer. **m–p** Wavenumber spectra of generated SAW fields. The white curves represent the theoretical wavenumber contour at 18.8 MHz. The first to fourth columns show the results of generating a long SAW jet near a PIM, a long SAW jet far from a PIM, an off-center SAW jet, and twin jets, respectively.

shifted, its spectrum becomes asymmetric with higher intensity in the region with $k_x < 0$ (Fig. 3o).

In addition to demonstrating single SAW jets, we fabricated a PIM (Fig. 3d) capable of generating a pair of long, narrow jets (referred to as twin jets), which, to the best of our knowledge, has not been achieved before. This PIM minimizes the SAW energy along the centerline through destructive interference, thus allowing for splitting a SAW jet into two lobes to create twin jets. Here, energy minimization is achieved by introducing an additional phase change of π rad to half of the PIM originally designed to generate a single SAW jet. The experimental SAW intensity field in Fig. 3l (right) confirms the generation of a pair of slim SAW jets (*i.e.*, twin jets) with a low energy region confined between them. The wavenumber spectrum in Fig. 3p for twin jets shows two high-intensity regions that are nearly symmetric to the k_y -axis, in contrast to the single jet's wavenumber spectrum in Fig. 3m. Additionally, we found that after splitting a single jet into twin jets, the width of each split jet becomes smaller than that of the original. However, as the device span increases, this effect gradually diminishes, as shown in Supplementary Fig. 7l.

The above analytical and experimental results demonstrate the ability to generate a single long SAW jet and twin jets using PIMs whose electrode shapes are encoded with customized spatial-varying phase profiles. Moreover, by optimizing the interdigital electrode configuration, PIMs can be developed to generate SAW jets with customized beam lengths and positions. Furthermore, compared to a traditional focused IDT with concentric arc-shaped electrodes, a PIM with the same span (W), number of electrodes (N), and center electrode focal length (d_c) can generate a significantly longer focused SAW beam, although its width slightly increases, as shown in Supplementary Fig. 8. Additionally, the four SAW fields (Fig. 3i–l, left) simulated using our analytical approach described in Supplementary Note 1 closely

resemble their corresponding experimental SAW fields (Fig. 3i–l, right). The beam widths measured from the experimental SAW fields are also close to those obtained from the simulation results (see Supplementary Fig. 9 for beam width comparisons), except for the case in Fig. 3k, which may be attributed to SAW field measurement and device fabrication errors. These results indicate that our analytical model is effective in predicting complex SAW jets generated by PIMs, thereby facilitating the design of PIM devices.

Transformation and ‘diode-like’ transmission of on-chip surface acoustic waves (SAWs)

Acoustic metamaterials are attracting increasing attention for transforming incident acoustic waves by modulating the phase and amplitude profiles of waves transmitted through them, as well as for achieving “diode-like” transmission of acoustic waves, *i.e.*, one-way routing^{79–82}. However, most studies focus on manipulating low-frequency acoustic waves such as bulk waves in air, fluids, and solids. Few studies have realized metamaterials capable of transforming the energy field of SAWs into desired patterns. Moreover, few studies have developed metamaterials that can both transform on-chip SAWs and achieve “diode-like” wave transmission.

To address these limitations, we have developed SAW metamaterial chips (illustrated in Fig. 1f) that can both transform incident SAW fields into desired patterns and achieve ‘diode-like’ routing. Our SAW metamaterial chip is composed of four key modules: (i) a straight electrode IDT, (ii) a lossy material (*e.g.*, high-damping paste or polymer) bonded on the substrate for absorbing SAWs as proven by experimental results in Supplementary Fig. 10, (iii) a one-way gain module (*e.g.*, amplification circuit) for signal amplification and breaking symmetry, as well as (iv) a PIM for emitting transformed SAWs. In the forward direction, an incident SAW is first received by the left-side

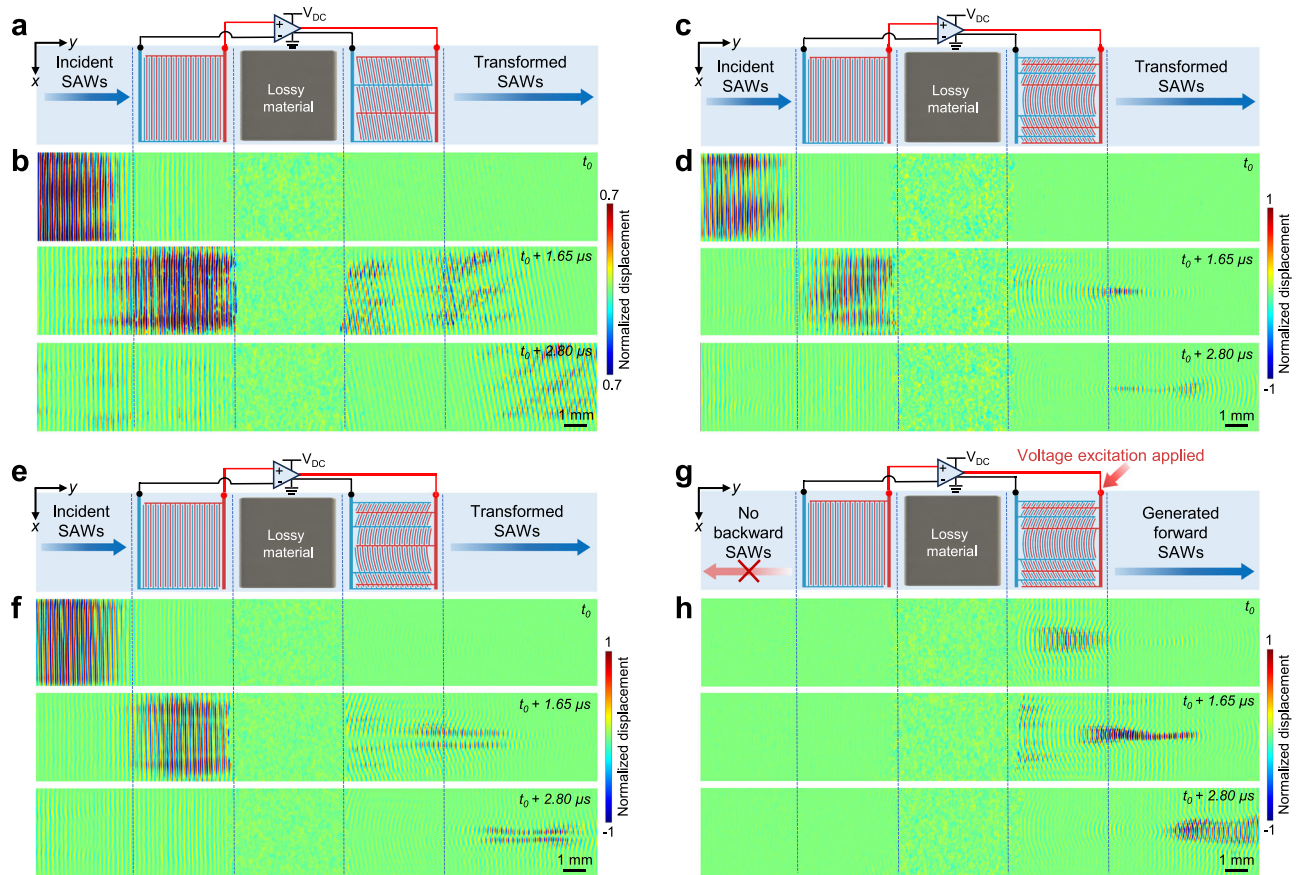


Fig. 4 | Results of transforming incident surface acoustic waves (SAWs) into waves with different wavefronts and energy patterns. a Chip design and **(b)** acquired SAW fields for steering straight-wavefront SAWs propagating in the $+y$ -direction to a direction 10 deg off the $+y$ -axis. **c** Chip design and **(d)** acquired SAW

fields for transforming straight-wavefront SAWs to a focused SAW jet. **e** Chip design and **(f)** acquired SAW fields for transforming straight-wavefront SAWs to twin jets. **g** Chip design and **(h)** acquired SAW fields showing that backward transmission of SAWs is prohibited.

straight-electrode IDT, generating an electrical signal that is amplified by the one-way gain module. The amplified voltage signal is then sent to the PIM to emit a transformed SAW to the right side of the chip. Through this process, an incident SAW can be transformed into a SAW with the desired wavefront/energy pattern, which depends on the PIM design. In the backward direction, a SAW incoming from the right side of the chip is first received by the PIM, producing an electrical signal. However, this signal cannot be delivered to the left-side straight-electrode IDT, due to the one-way amplification circuit. In addition, the SAW propagating in the $-y$ -direction cannot transmit through the piezoelectric substrate to the left side of the chip because the on-substrate high-damping lossy material absorbs SAWs.

For validation, we fabricated and characterized three SAW transformation chips having different PIM designs (see Fig. 4a, c, and e). When using the design in Fig. 4a, the acquired SAW displacement fields in Fig. 4b and Supplementary Movie. 1 reveal that incident SAWs propagating in the $+y$ -direction can be steered to a direction 10 deg off the $+y$ -axis. When using the chip design in Fig. 4c, the incident straight-wavefront SAWs are transformed into a focused SAW jet, as shown by the acquired displacement fields in Fig. 4d and Supplementary Movie. 2. Moreover, using the chip design in Fig. 4e, the incident SAWs are transformed into twin jets, as shown in Fig. 4f and Supplementary Movie. 3. In addition, the “diode-like” SAW transmission capability has been validated. The acquired SAW displacement fields in Fig. 4h and Supplementary Movie. 4 show that SAWs generated on the right side of the chip cannot transmit to the left side. The acquired transmission spectra in Supplementary Fig. 11 further confirm the ‘diode-like’ high transmission in the forward direction and nearly zero transmission in

the backward direction. By reversing the amplification circuit, backward high transmission can be achieved, while prohibiting forward transmission. Therefore, as validated by our experimental results in Fig. 4 and Supplementary Fig. 11, our developed SAW metamaterial chips enable the transformation of incident SAW fields into desired patterns, as well as the ‘diode-like’ delivery of the information carried by SAWs. Additionally, since the chip uses an IDT positioned to the left of the lossy material for SAW sensing, a small portion of the incident SAW energy ($\sim 9.3\%$, according to experimental results) is reflected. The IDT’s inherent filtering capability allows for frequency-selective SAW transmission. By replacing the sensing IDT with differently shaped sensing electrodes, it may be possible to reduce SAW reflections and enable multi-frequency or broadband SAW transmission – an interesting direction for future investigation.

Phased interdigital metamaterials (PIMs) for acoustofluidics

Acoustofluidics has shown great potential for generating and controlling fluid flows, as well as arranging and transporting micro/nano-objects in fluids. In recent years, these acoustofluidic abilities have been increasingly used for developing lab-on-a-chip devices for biomedical research and applications such as rotating cells, separating bioparticles, concentrating exosomes, as well as transporting and mixing biofluids^{14–25}. Here, we demonstrate that our PIMs can be used for acoustofluidics by enabling acoustic streaming to manipulate fluids and applying forces on micro/nanoparticles to transport and arrange them. The acoustofluidic experiments were performed using setups illustrated in Supplementary Fig. 12, with particle distributions and motions recorded by a camera.

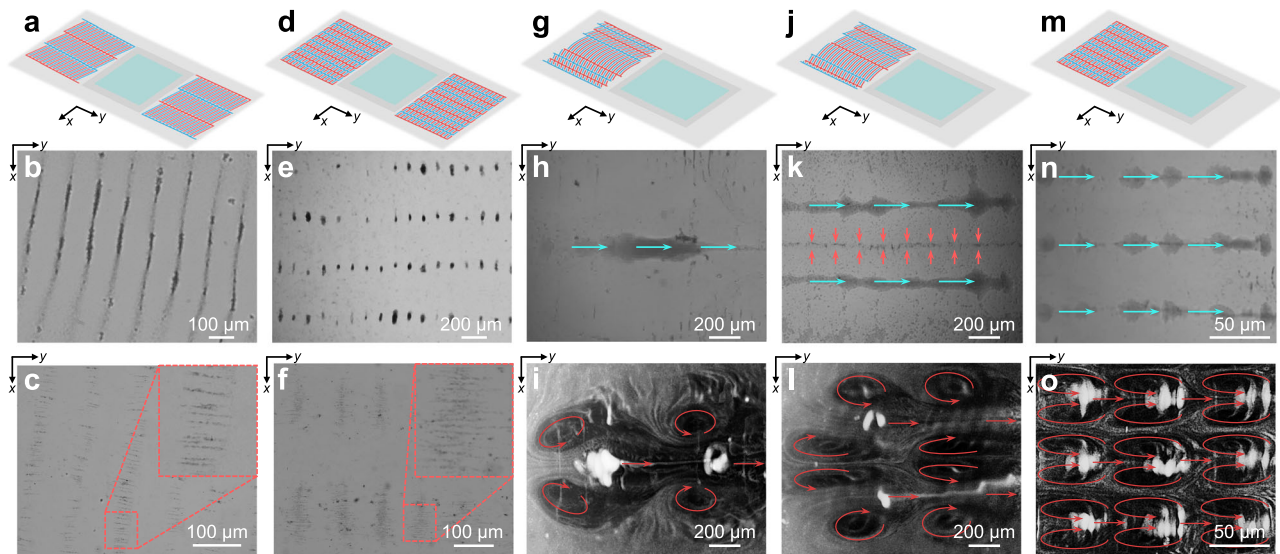


Fig. 5 | Experimental results showing acoustofluidic phenomena achieved by phased interdigital metamaterials (PIMs). **a** Chip design and **(b, c)** results of patterning 35 μm SiO_2 microparticles and multi-walled carbon nanotubes (MWCNTs) using tilted standing surface acoustic waves (SAWs) generated by a pair of PIMs. **d** Chip design and **(e, f)** results of patterning microparticles and MWCNTs using pseudo-standing SAWs generated by a pair of PIMs. **g** Chip design and **(h, i)**

results of transporting 35 μm and 550 nm SiO_2 microparticles using a focused SAW energy beam. **j** Chip design and **(k, l)** results of transporting 35 μm and 550 nm SiO_2 microparticles using a pair of focused SAW beams. **m** Chip design and **(n, o)** results of transporting 35 μm and 550 nm SiO_2 microparticles using three energy beams of pseudo-standing SAWs.

When using a pair of PIMs for generating tilted standing SAWs, the acquired microscopic image in Fig. 5b and Supplementary Movie. 5 show that 35 μm SiO_2 particles are arranged in a tilted, parallel-line-like distribution, as these microparticles are trapped by the potential valleys of the generated tilted standing SAWs. Interestingly, microparticles can be arranged in a 2D lattice-like pattern (see Fig. 5e and Supplementary Movie. 6), when using a pair of PIMs designed for generating pseudo-standing SAWs. Previous approaches for constructing 2D lattice-like particle patterns typically required orthogonally arranged IDTs that generated SAWs propagating along orthogonal axes; however, our PIM-based approach requires only SAWs propagating along a single axis, which has not been presented before to the best of our knowledge. Since SAWs generated on a piezoelectric wafer are accompanied by dynamic electric fields, we also demonstrated the ability of our PIMs for arranging MWCNTs using the accompanied electric fields. When using tilted standing SAWs, MWCNTs align perpendicular to the node lines, forming multiple parallel groups in the potential valleys of the tilted standing SAWs, as shown by the acquired microscopic image in Fig. 5c. When using pseudo-standing SAWs, MWCNTs align along the SAW propagation direction, forming multiple groups (see Fig. 5f) in SAW potential valleys with a 2D lattice-like distribution. Additionally, the arrangements of microparticles and MWCNTs observed in the above experiments can be predicted using analytically simulated SAW-induced acoustic radiation and dielectrophoretic force fields, respectively (see Supplementary Note 1 and Fig. 13 for the simulation approach and results, respectively).

In addition to arranging the distributions of micro/nano-objects, we demonstrated the ability to transport particles, as well as generate unique fluid streaming fields. First, when using a PIM to generate a long narrow SAW beam, Fig. 5h and Supplementary Movie 7 show that 35 μm SiO_2 particles were transported along the SAW beam, primarily by the acoustic radiation force. The acoustic streaming pattern (Fig. 5i), observed through 500 nm SiO_2 particles influenced mainly by the streaming-induced drag force, revealed a microscale jet flow accompanied by multiple pairs of counter-chirality vortices symmetric to the jet (Supplementary Fig. 14d and Movie. 8). Interestingly, this flow pattern resembles the classical free in-air subsonic jet with an array of

vortices⁸³, but here it is observed in a microscale liquid environment on a piezoelectric chip. Second, when using a PIM to generate two long narrow SAW beams, 35 μm particles were transported along the two SAW beams (see Fig. 5k and Supplementary Movie. 9), with some microparticles trapped along the centerline between the two SAW beams due to minimal SAW potential from destructive interference. The streaming pattern (Fig. 5l) revealed by 500 nm particles shows that each high-potential SAW beam induced a forward flow with counter-chirality streaming vortices on different sides, and interestingly, the combined effect of inner vortices created a backward flow along the low-potential centerline between the two SAW beams (Supplementary Fig. 14e and Movie. 10). Third, when using a PIM to generate pseudo-standing SAWs with multiple high-intensity beams, 35 μm particles were transported by these high-intensity beams (Fig. 5n and Supplementary Movie. 11). Moreover, each SAW beam induced a forward streaming flow with multiple pairs of counter-chirality streaming vortices on different sides (Supplementary Fig. 14f and Movie. 12). Their combination created an array of periodically arranged streaming vortices (Fig. 5o), having the same chirality along the +y-direction and alternating chirality in the +x-direction.

Discussion

In this study, we have developed and validated PIMs, which enable versatile transformation of SAWs on piezoelectric chips, “diode-like” transmission of SAW information, generation of fluid streaming vortices, as well as manipulation of micro/nano-objects. The PIMs have complex interdigital electrodes, whose shapes are encoded with pre-determined position-dependent phase profiles, enabling the ability to generate SAWs with desired wavefronts and energy patterns, such as SAWs propagating in a desired direction, pseudo-standing SAWs, long single SAW jets, and twin jets. These PIMs open unique pathways for developing metamaterial chips to control on-chip SAWs and for designing acoustofluidic devices to manipulate fluids and micro/nano-objects. Based on PIMs, on one hand, we have developed SAW chips, which are able to transform forward-propagation SAWs into waves having the desired wavefronts and energy patterns, as well as achieve “diode-like” delivery of SAW information by forbidding the

transmission of the information carried by backward-propagation SAWs. On the other hand, we successfully demonstrated multiple acoustofluidic functions using PIMs, such as arranging micro-objects into different patterns, generating streaming vortices, and manipulating nano-objects.

Traditional IDTs for SAW generation have simple configurations, such as an array of parallelly arranged electrodes for generating straight-wavefront SAWs. This study breaks the limitation by offering a generalized approach for designing a customized PIM with complex-shaped interdigital electrodes, whose geometries are encoded with the desired position-dependent phase function $\phi_d(x)$. Supplementary Fig. 15 compares the SAW fields generated by our PIM and a phased array composed of numerous elements along straight lines, with excitation phases satisfying the same phase function $\phi_d(x)$. Notably, these SAW fields are nearly identical when the observation distance exceeds three wavelengths from the source. This indicates that our PIM, with its complex-shaped electrodes, can produce a SAW field nearly identical to that of the phased array, without requiring the complex multi-channel excitation system needed to supply different signals to individual elements of the phased array.

An analytical approach considering the direction-dependent SAW speed has been developed for quickly predicting SAWs generated by a PIM with complex electrodes, as well as providing guidance for PIM design and optimization. Compared to the multiphysics finite element method, our analytical approach significantly reduces computation time while producing SAW fields that closely match those from finite element models with a fine mesh size of $\lambda/8$ (see Supplementary Note 3 and Figs. 16 and 17). Although the finite element method is a more generalized approach capable of addressing diverse wave propagation problems and capturing more detailed features (*e.g.*, geometry, material properties, and boundary conditions) of the SAW chip, our analytical approach is more efficient for its intended purpose: predicting SAW fields generated by PIMs with complex-shaped electrodes. In addition, the SAW fields predicted by our analytical model agree well with experimental results measured by laser Doppler vibrometry, as validated by multiple tests with SAW propagating in different directions, pseudo-standing SAWs, and single and twin SAW jets.

Although various metamaterials have been developed for controlling low-frequency acoustic waves in air, fluids, and solids, designing metamaterials for on-chip SAWs remains challenging^{79–82}. Few studies realize metamaterials that can both transform on-chip SAWs and achieve “diode-like” delivery of SAW information. This study addresses these challenges by developing unique SAW metamaterial chips with four key components: a straight-electrode IDT deposited on a piezoelectric substrate, a high-damping paste-based lossy material attached on the piezoelectric substrate, an amplification circuit-based gain module, and a PIM. The laser vibrometry-based validation tests show that our manufactured chips can transform forward-propagation SAWs into waves with desired wavefronts and energy distributions, such as SAWs with a steered propagation direction, energy-focused long jet beams, and twin jet beams. Additionally, the laser vibrometry-based validation study shows that the information carried by forward-propagation SAWs transmits through the chip, while backward SAW information delivery is blocked.

This research introduces unique SAW energy patterns, including a long SAW jet, twin SAW jets, and pseudo-standing SAWs, analyzes their space-domain patterns and wavenumber-domain spectra, and investigates their abilities for acoustofluidics. The high-frequency (*e.g.*, tens of megahertz) long SAW jet has highly focused SAW energy in a long beam with an FWHM value smaller than a wavelength. This breaks the limit of previous studies focusing on acoustic jets at low frequencies^{68–70}. Our twin SAW jets, which have a pair of long SAW jets very close to each other in the space domain and a pair of wavenumber components in the space domain, fill the gap of previous studies

limited to single jets. Furthermore, compared to previous studies using acoustic jets for sensing applications, we demonstrated the ability of acoustic jets for acoustofluidics, such as generating streaming vortices and manipulating micro/nano-objects. In addition to SAW jets, this study introduces and analyzes pseudo-standing SAWs, which are formed by the interference of traveling SAWs generated by a single-side PIM, and their ability for manipulating micro/nano-objects is successfully demonstrated. Our numerical and experimental results show that a pseudo-standing SAW has a similar energy pattern compared to a regular standing SAW generated by a pair of counter-direction straight-electrode IDTs. Moreover, the period of SAW node lines depends on the PIM's electrode design instead of the SAW wavelength, while this parameter in regular standing SAWs equals half a wavelength. Furthermore, the pseudo-standing SAW can arrange micro/nano-objects into parallel-line-like patterns, as validated by the microscopic images of acoustofluidic experiments.

Despite the successful demonstrations described above, the PIMs presented in this study still have several limitations, including the inability to control SAWs propagating in multiple directions and the lack of control over SAWs at multiple frequencies or across a wide frequency band. Looking ahead, we plan to design PIMs with electrode geometries different from those presented in this paper, aiming to generate other intriguing on-chip SAW patterns, control SAWs propagating in multiple directions, enable wideband operation, and increase device frequencies. Note that additional challenges arise as design frequencies enter the gigahertz range. Device fabrication becomes more complex and costly because interdigital electrode widths and spacings are reduced to the submicron regime, necessitating high-resolution lithography (*e.g.*, electron-beam lithography). In addition, thermal drift (*e.g.*, temperature-induced resonance frequency shift) becomes more pronounced, thereby requiring strategies for device temperature control.

In a nutshell, this study advances the fields of SAW chips, metamaterials, and acoustofluidics, by introducing a unique approach to develop PIMs with complex-shaped interdigital electrodes to generate on-chip SAWs with desired wavefronts and energy distributions, as well as by developing PIMs that can generate pseudo-standing SAWs, single long SAW jets, and twin SAW jets. These PIMs enable novel metamaterials for transforming on-chip SAWs and “diode-like” transmission of SAW information, and they enable acoustofluidic functions such as generating streaming vortices and contactless manipulation of micro/nano-objects. Beyond these demonstrated functions, we will continue exploring the potential functions of PIMs, such as patterning cells, concentrating bioparticles, rotating cells, and stimulating cells. With unique capabilities of manipulating SAWs, microfluids, and micro/nano-objects, we expect this study can inspire researchers for the development of future SAW metamaterials for quantum acoustics, optomechanics, signal processing chips, as well as acoustofluidic devices for chemical and biomedical applications.

Methods

Simulation of surface acoustic waves (SAWs) generated by phased interdigital metamaterials (PIMs)

To predict the wavefields of SAWs generated by PIMs with complex-shaped electrodes, an analytical model was established. The details of the analytical model are given in Supplementary Note 1, and a schematic of the analytical model is shown in Supplementary Fig. 1. Since the performance of a SAW device is influenced by both the electrode design and the anisotropic material properties of the piezoelectric substrate, our model considers both the geometries of complex-shaped interdigital electrodes as well as the direction-dependent SAW velocity and electromechanical potential-to-displacement ratio. Based on the analytical model, we can predict the displacement, electric potential, and intensity fields of SAWs generated by PIMs. Using these fields, the SAW-induced acoustic radiation and dielectrophoretic

forces acting on small particles can then be analyzed, as detailed in Supplementary Note 1, enabling the prediction of their arrangement within the generated SAW field.

Design and manufacturing of phased interdigital metamaterials (PIMs)

To design a PIM for generating SAWs with desired wavefronts and energy distributions, a subwavelength-resolution spatial-varying phase profile $\phi_d(x)$ needs to be determined and then encoded into the electrode configuration. Supplementary Note 2 gives the expressions of the desired phase profiles for generating tilted SAWs, pseudo-standing SAWs, a SAW jet, and twin jets. It also provides the relation to encode the desired phase profile into the interdigital electrode's profile. Based on the approach in Supplementary Note 2, we designed customized electrode patterns for different PIMs with a working frequency of 18.8 MHz (see Supplementary Fig. 3 for all the phase profiles, electrode configurations, and photos of fabricated devices). To manufacture these PIMs, we deposited a 10 nm layer of chromium (Cr) and then an 80 nm layer of gold (Au) on a 0.5 mm-thick Y128-cut LiNbO₃ substrate using procedures including spin coating, lithography, e-beam evaporation, lift-off, etc.

For the transformation and 'diode-like' transmission of SAWs, we fabricated devices each integrating a SAW chip and a one-way amplification circuit (see Supplementary Fig. 18 for the schematic and photo of a device). The circuit consists of a BGA 2869 amplification chip (NXP Semiconductors), a 220 Ω resistor (R), and four 400 nF capacitors (C_1 , C_2 , C_3 , and C_4). Its operational frequency range spans from 0.1 MHz to 2 GHz. To ensure stable amplification without noticeable nonlinear waveform distortion, the input signal at the signal-in port and the direct current (DC) voltage bias at the V_{DC} port were kept below 1 V and 12 V, respectively. The signal-in port is connected to the straight-electrode IDT, allowing the SAW signals acquired by the IDT to be fed into the circuit. The amplified signal at the signal-out port is supplied to the PIM transducer for SAW generation. To generate SAWs with varying displacements, the output voltage at the signal-out port can be adjusted by varying the DC voltage bias applied to the amplification circuit. In this study, a DC voltage bias of 9 V was used to generate SAWs strong enough for reliable measurement using a laser Doppler vibrometer.

Acquisition of surface acoustic wave (SAW) fields

To measure SAW fields generated by a PIM, we used a customized laser Doppler vibrometry setup illustrated in Supplementary Fig. 4. A function generator (DGI022, Rigol) is used to generate a Hanning window modulated multi-cycle sine signal with a center frequency matching the IDT's resonance frequency (18.8 MHz). This excitation signal is sent to the IDT for SAW generation. A laser Doppler vibrometer (FX-1-130, Polytec Inc.) is used to acquire SAWs propagating on the piezoelectric substrate based on the Doppler effect. The laser beam is focused on the top surface of the piezoelectric wafer, and it is perpendicular to the wafer for measuring the generated SAW's out-of-plane displacement component. The output voltage signal from the laser Doppler vibrometer is recorded by an oscilloscope (TDS 2014C, Tektronix). By using the laser Doppler vibrometer's decoder information (10 nm/V), the measured voltages are converted to out-of-plane displacements of SAWs. To acquire a time-space wavefield of generated SAWs, a point-by-point scanning approach is performed, by gradually changing the laser position and acquiring displacement waveforms. At each scanning position, the measurement is repeated eight times to acquire eight waveforms, which are averaged to obtain a denoised waveform. By combining the denoised waveforms acquired at all scanning positions within the desired SAW measurement region, a time-space wavefield $u(t, \mathbf{x})$ containing the information of the SAW propagation can be obtained. By further applying Fourier transform to the time-space wavefield, a

frequency-space wavefield $U(f, \mathbf{x})$ is obtained. The SAW intensity field $I(f, \mathbf{x})$ at a selected frequency of f_i is evaluated using $|U(f_i, \mathbf{x})|^2$. The cumulative SAW energy field is evaluated with the relation $E(\mathbf{x}) = \int |H(t, \mathbf{x})|^2 dt$, where $H(t, \mathbf{x})$ is obtained through the Hilbert transform of the wavefield $u(t, \mathbf{x})$. To analyze the wavenumber content of the generated SAWs, the 2D Fourier transform is applied to the frequency-space wavefield $U(f, \mathbf{x})$, yielding the frequency-wavenumber spectrum $S(f, \mathbf{k})$. The spectrum at a selected frequency f_i is then extracted and plotted in the k_x - k_y wavenumber space, as illustrated in Supplementary Fig. 4. From the resulting wavenumber-domain spectrum, the key wavenumber components of the generated SAWs can be analyzed.

Procedures of acoustofluidic experiments

To validate the ability of our PIMs for arranging micro/nano-objects and generating fluid streaming, multiple acoustofluidic experiments were performed. As shown in Supplementary Fig. 12, a continuous sine signal at a frequency matching the PIM's resonance frequency was generated by an arbitrary function generator (FG3052C, Tektronix), amplified by a power amplifier (A075, E&I), and then sent to the PIM for generating SAWs. A small microfluidic chamber was attached to the LiNbO₃ substrate and loaded with deionized water containing micro/nano-objects, such as 35 μm SiO₂ microparticles, MWCNTs, and 550 nm SiO₂ nanoparticles. The SAW device with the microfluidic chamber is placed on the translation stage of an inverted microscope (TE2000-U, Nikon) to observe the object manipulation process. A camera is used to capture microscopic images and record movies during and after the SAW-based object manipulation. To visualize the fluid streaming, the acquired time-sequential images were stacked together.

Data availability

Relevant data supporting the key findings of this study are available within the article and the Supplementary Information file. All raw data generated during the current study are available from the corresponding authors upon request.

References

- Hermelin, S. et al. Electrons surfing on a sound wave as a platform for quantum optics with flying electrons. *Nature* **477**, 435–438 (2011).
- McNeil, R. P. G. et al. On-demand single-electron transfer between distant quantum dots. *Nature* **477**, 439–442 (2011).
- Manenti, R. et al. Circuit quantum acoustodynamics with surface acoustic waves. *Nat. Commun.* **8**, 975 (2017).
- Gustafsson, M. V. et al. Propagating phonons coupled to an artificial atom. *Science* **346**, 207–211 (2014).
- Wang, C. et al. Integrated lithium niobate electro-optic modulators operating at CMOS-compatible voltages. *Nature* **562**, 101–104 (2018).
- Balam, K. C., Davanço, M. I., Song, J. D. & Srinivasan, K. Coherent coupling between radiofrequency, optical and acoustic waves in piezo-optomechanical circuits. *Nat. Photonics* **10**, 346–352 (2016).
- Fuhrmann, D. A. et al. Dynamic modulation of photonic crystal nanocavities using gigahertz acoustic phonons. *Nat. Photonics* **5**, 605–609 (2011).
- Tadesse, S. A. & Li, M. Sub-optical wavelength acoustic wave modulation of integrated photonic resonators at microwave frequencies. *Nat. Commun.* **5**, 5402 (2014).
- Wiele, C., Haake, F., Rocke, C. & Wixforth, A. Photon trains and lasing: the periodically pumped quantum dot. *Phys. Rev. A* **58**, R2680–R2683 (1998).
- Morgan D. *Surface Acoustic Wave Filters With Applications to Electronic Communications and Signal Processing* 2nd edn (Academic Press (2007).

11. Andrew et al. The 2019 surface acoustic waves roadmap. *J. Phys. D: Appl. Phys.* **52**, 1–40 (2019).
12. Stern, A., Efimkin, D. K., Galitski, V., Fisk, Z. & Xia, J. Radio frequency tunable oscillator device based on a SmB6 microcrystal. *Phys. Rev. Lett.* **116**, 166603 (2016).
13. Takai, T. et al. High-performance SAW resonator on new multi-layered substrate using LiTaO₃ crystal. *IEEE Trans. Ultrason. Ferroelectr. Freq. Control* **64**, 1382–1389 (2017).
14. Ozcelik, A. et al. Acoustic tweezers for the life sciences. *Nat. Methods* **15**, 1021–1028 (2018).
15. Rufo, J., Cai, F., Friend, J., Wiklund, M. & Huang, T. J. Acoustofluidics for biomedical applications. *Nat. Rev. Methods Prim.* **2**, 30 (2022).
16. Yang, S. et al. Harmonic acoustics for dynamic and selective particle manipulation. *Nat. Mater.* **21**, 540–546 (2022).
17. Collins, D. J. et al. Acoustic tweezers via sub-time-of-flight regime surface acoustic waves. *Sci. Adv.* **2**, e1600089 (2016).
18. Riaud, A., Baudoin, M., Matar, O. B., Becerra, L. & Thomas, J. L. Selective manipulation of microscopic particles with precursor swirling Rayleigh waves. *Phys. Rev. Appl.* **7**, 024007 (2017).
19. Baudoin, M. et al. Folding a focalized acoustical vortex on a flat holographic transducer: Miniaturized selective acoustical tweezers. *Sci. Adv.* **5**, eaav1967 (2019).
20. Marx, V. Biophysics: using sound to move cells. *Nat. Methods* **12**, 41–44 (2015).
21. Reboud, J. et al. Shaping acoustic fields as a toolset for microfluidic manipulations in diagnostic technologies. *Proc. Natl. Acad. Sci. USA* **109**, 15162–15167 (2012).
22. Yeo, L. Y. & Friend, J. R. Surface acoustic wave microfluidics. *Annu. Rev. Fluid Mech.* **46**, 379–406 (2014).
23. Friend, J. & Yeo, L. Y. Microscale acoustofluidics: Microfluidics driven via acoustics and ultrasonics. *Rev. Mod. Phys.* **83**, 647–704 (2011).
24. Baudoin, M. & Thomas, J.-L. Acoustic tweezers for particle and fluid micromanipulation. *Annu. Rev. Fluid Mech.* **52**, 205–234 (2020).
25. Meng, L. et al. Acoustic tweezers. *J. Phys. D Appl. Phys.* **52**, 273001 (2019).
26. Fu, Y. Q. et al. Advances in piezoelectric thin films for acoustic biosensors, acoustofluidics and lab-on-chip applications. *Prog. Mater. Sci.* **89**, 31–91 (2017).
27. Lamanna, L., Rizzi, F., Bhethanabotla, V. R. & De Vittorio, M. Conformable surface acoustic wave biosensor for E-coli fabricated on PEN plastic film. *Biosens. Bioelectron.* **163**, 112164 (2020).
28. Agostini, M. & Cecchini, M. Ultra-high-frequency (UHF) surface-acoustic-wave (SAW) microfluidics and biosensors. *Nanotechnology* **32**, 312001 (2021).
29. Shilton, R. J., Travagliati, M., Beltram, F. & Cecchini, M. Nanoliter-droplet acoustic streaming via ultra high frequency surface acoustic waves. *Adv. Mater.* **26**, 4941–4946 (2014).
30. Collins, D. J. et al. Selective particle and cell capture in a continuous flow using micro-vortex acoustic streaming. *Lab Chip* **17**, 1769–1777 (2017).
31. Ahmed, H., Destgeer, G., Park, J., Afzal, M. & Sung, H. J. Sheathless focusing and separation of microparticles using tilted-angle traveling surface acoustic waves. *Anal. Chem.* **90**, 8546–8552 (2018).
32. Destgeer, G. et al. Microparticle self-assembly induced by travelling surface acoustic waves. *RSC Adv.* **9**, 7916–7921 (2019).
33. Nam, H., Sung, H. J., Park, J. & Jeon, J. S. Manipulation of cancer cells in a sessile droplet via travelling surface acoustic waves. *Lab Chip* **22**, 47–56 (2022).
34. Lenshof, A., Magnusson, C. & Laurell, T. Acoustofluidics 8: Applications of acoustophoresis in continuous flow microsystems. *Lab Chip* **12**, 1210–1223 (2012).
35. Chen, C. et al. Acoustofluidic rotational tweezing enables high-speed contactless morphological phenotyping of zebrafish larvae. *Nat. Commun.* **12**, 1118 (2021).
36. Zhang, P. et al. Contactless, programmable acoustofluidic manipulation of objects on water. *Lab Chip* **19**, 3397–3404 (2019).
37. Gedge, M. & Hill, M. Acoustofluidics 17: theory and applications of surface acoustic wave devices for particle manipulation. *Lab Chip* **12**, 2998–3007 (2012).
38. Collins, D. J. et al. Two-dimensional single-cell patterning with one cell per well driven by surface acoustic waves. *Nat. Commun.* **6**, 8686 (2015).
39. Guo, F. et al. Three-dimensional manipulation of single cells using surface acoustic waves. *Proc. Natl. Acad. Sci. USA* **113**, 1522–1527 (2016).
40. Naseer, S. M. et al. Surface acoustic waves induced micropatterning of cells in gelatin methacryloyl (GelMA) hydrogels. *Biofabrication* **9**, 015020 (2017).
41. Antfolk, M. & Laurell, T. Continuous flow microfluidic separation and processing of rare cells and bioparticles found in blood – a review. *Anal. Chim. Acta* **965**, 9–35 (2017).
42. Baudoin, M. et al. Spatially selective manipulation of cells with single-beam acoustical tweezers. *Nat. Commun.* **11**, 4244 (2020).
43. Wu, M. et al. Isolation of exosomes from whole blood by integrating acoustics and microfluidics. *Proc. Natl. Acad. Sci. USA* **114**, 10584–10589 (2017).
44. Zhang, P. et al. Acoustoelectronic nanotweezers enable dynamic and large-scale control of nanomaterials. *Nat. Commun.* **12**, 3844 (2021).
45. Naquin, T. D. et al. Acoustic separation and concentration of exosomes for nucleotide detection: ASCENDx. *Sci. Adv.* **10**, eadm8597 (2024).
46. Tan, M. K., Friend, J. R. & Yeo, L. Y. Interfacial Jetting Phenomena Induced by Focused Surface Vibrations. *Phys. Rev. Lett.* **103**, 024501 (2009).
47. Li, P. et al. Detachable acoustophoretic system for fluorescence-activated sorting at the single-droplet level. *Anal. Chem.* **91**, 9970–9977 (2019).
48. Lanoy, M. et al. Subwavelength focusing in bubbly media using broadband time reversal. *Phys. Rev. B* **91**, 6 (2015).
49. Li, P.-Q. et al. Holographic surface-acoustic-wave tweezers for functional manipulation of solid or liquid objects. *Phys. Rev. Appl.* **20**, 064003 (2023).
50. Tian, Z. et al. Generating multifunctional acoustic tweezers in petri dishes for contactless, precise manipulation of bioparticles. *Sci. Adv.* **6**, eabb0494 (2020).
51. O’Rourke, R., Winkler, A., Collins, D. & Ai, Y. Slowness curve surface acoustic wave transducers for optimized acoustic streaming. *RSC Adv.* **10**, 11582–11589 (2020).
52. Zhang, N. et al. Microliter ultrafast centrifuge platform for size-based particle and cell separation and extraction using novel omnidirectional spiral surface acoustic waves. *Lab Chip* **21**, 904–915 (2021).
53. Gu, Y. et al. Acoustofluidic centrifuge for nanoparticle enrichment and separation. *Sci. Adv.* **7**, eabc0467 (2021).
54. Kang, P. et al. Acoustic tweezers based on circular, slanted-finger interdigital transducers for dynamic manipulation of micro-objects. *Lab Chip* **20**, 987–994 (2020).
55. Cha, J., Kim, K. W. & Daraio, C. Experimental realization of on-chip topological nanoelectromechanical metamaterials. *Nature* **564**, 229–233 (2018).
56. Zhang, Z.-D. et al. Topological surface acoustic waves. *Phys. Rev. Appl.* **16**, 044008 (2021).
57. Dehghanasiri, R., Eftekhari, A. A. & Adibi, A. Hypersonic surface phononic bandgap demonstration in a CMOS-compatible pillar-

- based piezoelectric structure on silicon. *Phys. Rev. Appl.* **10**, 064019 (2018).
58. Ash, B. J., Worsfold, S. R., Vukusic, P. & Nash, G. R. A highly attenuating and frequency tailorable annular hole phononic crystal for surface acoustic waves. *Nat. Commun.* **8**, 174 (2017).
59. Xu, M. et al. Nonreciprocal surface acoustic wave propagation via magneto-rotation coupling. *Sci. Adv.* **6**, eabb1724 (2020).
60. Shao, L. et al. Non-reciprocal transmission of microwave acoustic waves in nonlinear parity–time symmetric resonators. *Nat. Electron.* **3**, 267–272 (2020).
61. Shen, C. et al. Electrically tunable surface acoustic wave propagation at MHz frequencies based on carbon nanotube thin-film transistors. *Adv. Funct. Mater.* **31**, 2010744 (2021).
62. Yan, M. et al. On-chip valley topological materials for elastic wave manipulation. *Nat. Mater.* **17**, 993–998 (2018).
63. Bandhu, L. & Nash, G. R. Controlling the properties of surface acoustic waves using graphene. *Nano Res.* **9**, 685–691 (2016).
64. Wang, J.-Q. et al. Extended topological valley-locked surface acoustic waves. *Nat. Commun.* **13**, 1324 (2022).
65. Shao, L. et al. Electrical control of surface acoustic waves. *Nat. Electron.* **5**, 348–355 (2022).
66. Xu, M., Lee, P. V. S. & Collins, D. J. Microfluidic acoustic sawtooth metasurfaces for patterning and separation using traveling surface acoustic waves. *Lab Chip* **22**, 90–99 (2022).
67. Wang, W. et al. Experimental realization of on-chip surface acoustic wave metasurfaces at Sub-GHz. *Adv. Sci.* **12**, 2411825 (2025).
68. Zhao, L., Horiuchi, T. & Yu, M. Broadband ultra-long acoustic jet based on double-foci luneburg lens. *JASA Express Lett.* **1**, 114001 (2021).
69. Zhao, L., Bi, C., Huang, H., Liu, Q. & Tian, Z. A review of acoustic Luneburg lens: Physics and applications. *Mech. Syst. Signal Process.* **199**, 110468 (2023).
70. Lu, C. et al. GRIN metamaterial generalized Luneburg lens for ultra-long acoustic jet. *Appl. Phys. Lett.* **118**, 144103 (2021).
71. Marzo, A. et al. Holographic acoustic elements for manipulation of levitated objects. *Nat. Commun.* **6**, 8661 (2015).
72. Ghobrial, A., Cox, L., Caleap, M., Croxford, A. & Drinkwater, B. W. Realization of compact tractor beams using acoustic delay-lines. *Appl. Phys. Lett.* **110**, 014102 (2017).
73. Ortega-Sandoval, M. E. et al. Ultrasonic manipulation of particles and cell aggregates with simultaneous acoustic visualization. *Appl. Phys. Lett.* **124**, 204102 (2024).
74. Melde, K., Mark, A. G., Qiu, T. & Fischer, P. Holograms for acoustics. *Nature* **537**, 518–522 (2016).
75. Melde, K. et al. Acoustic fabrication via the assembly and fusion of particles. *Adv. Mater.* **30**, 1704507 (2018).
76. Ma, Z. et al. Acoustic holographic cell patterning in a biocompatible hydrogel. *Adv. Mater.* **32**, 1904181 (2020).
77. Kinsler J. E., Frey A. R., Coppens A. B., Sanders J. V. *Fundamentals of Acoustics* 4th edn (Wiley, 2000).
78. Ginzel, E. *Beam Width Analysis*. <https://www.laser-beam-profile.com/evaluation-of-the-laser-beam-width/> (2001).
79. Assouar, B. et al. Acoustic metasurfaces. *Nat. Rev. Mater.* **3**, 460–472 (2018).
80. Cummer, S. A., Christensen, J. & Alu, A. Controlling sound with acoustic metamaterials. *Nat. Rev. Mater.* **1**, 16001 (2016).
81. Ma, G. & Sheng, P. Acoustic metamaterials: From local resonances to broad horizons. *Sci. Adv.* **2**, e1501595 (2016).
82. Dong, E. et al. Underwater acoustic metamaterials. *Natl Sci. Rev.* **10**, nwc246 (2022).
83. Popiel, C. O. & Trass, O. Visualization of a free and impinging round jet. *Exp. Therm. Fluid Sci.* **4**, 253–264 (1991).

Acknowledgements

The authors acknowledge the financial support from the National Institute of General Medical Sciences of the National Institutes of Health (7R01GM144417), National Science Foundation (CMMI 2243771, CMMI 2340016, and CBET-2427828), and Nuclear Energy University Programs (DE-NE0009187). We also acknowledge the Advanced Research Computing unit at Virginia Tech for providing research computing infrastructure and support.

Author contributions

J.L. and L.B. conceived the idea. L.B. and T.L. performed the SAW field characterization experiments. L.B. and S.Y. manufactured the SAW devices. J.L., C.Q., and Y.D. performed the acoustofluidic experiments. T.L. and L.S. performed analytical simulations. S.Y. participated in the project discussion. All the authors contributed to the paper writing and revision. Z.T. provided research guidance and supervised the study.

Competing interests

The authors declare no competing interests.

Additional information

Supplementary information The online version contains supplementary material available at <https://doi.org/10.1038/s41467-025-66488-z>.

Correspondence and requests for materials should be addressed to Shujie Yang or Zhenhua Tian.

Peer review information *Nature Communications* thanks Andrea Achilleos, Taehwa Lee, Sriram Subramanian and the other anonymous reviewer(s) for their contribution to the peer review of this work. A peer review file is available.

Reprints and permissions information is available at <http://www.nature.com/reprints>

Publisher's note Springer Nature remains neutral with regard to jurisdictional claims in published maps and institutional affiliations.

Open Access This article is licensed under a Creative Commons Attribution-NonCommercial-NoDerivatives 4.0 International License, which permits any non-commercial use, sharing, distribution and reproduction in any medium or format, as long as you give appropriate credit to the original author(s) and the source, provide a link to the Creative Commons licence, and indicate if you modified the licensed material. You do not have permission under this licence to share adapted material derived from this article or parts of it. The images or other third party material in this article are included in the article's Creative Commons licence, unless indicated otherwise in a credit line to the material. If material is not included in the article's Creative Commons licence and your intended use is not permitted by statutory regulation or exceeds the permitted use, you will need to obtain permission directly from the copyright holder. To view a copy of this licence, visit <http://creativecommons.org/licenses/by-nc-nd/4.0/>.

© The Author(s) 2025